

A numerical free-surface condition for elastic/viscoelastic finite-difference modeling in the presence of topography

Johan O. A. Robertsson*

ABSTRACT

An accurate free-surface boundary condition is important for solving a wide variety of seismic modeling problems. In particular, for earthquake site studies or shallow environmental investigations the surface of the earth may have a significant impact on the outcome of simulations. Computations based on several elastic/viscoelastic flat horizontal free-surface conditions are compared and benchmarked against an analytical solution. An accurate and simple condition is found and then generalized to allow for irregular free surfaces. This new method is simple to implement in conventional staggered finite-difference schemes, is computationally efficient and enables modeling of highly irregular topography. The accuracy of the method is investigated and criteria for sampling of the wavefield are derived.

INTRODUCTION

Generally, the earth's surface is far from flat. Since this is usually the location at which seismic observations are made, topography may have a significant influence on recorded data. Topography does not pose a problem for finite-element methods. The ability to model complicated and irregular boundary conditions is one of the principal advantages of such methods. Finite-element methods are, however, rarely used to simulate seismic wave propagation problems because of the excessive computational costs in comparison with explicit finite-difference schemes (Strang and Fix, 1973; Cohen et al., 1993).

For finite-difference modeling of horizontal free surfaces, several authors have employed the implicit condition of Vidale and Clayton (1986), which although stable is limited to second-order accuracy. In a staggered scheme (Virieux, 1986), the free-surface condition becomes explicit, but problems with accuracy and convergence may arise. Levander (1988) proposed an

alternative flat free-surface implementation based on a so-called image method.

Jih et al. (1988) described a finite-difference method in which irregular free surfaces are decomposed into segments approximated by piecewise continuous lines. Following a predefined classification scheme, the different segments are treated using a one-sided difference approximation of the free-surface condition. Frankel and Leith (1992) modeled the topographic effects on seismic waves generated by a hypothetical nuclear explosion at a Russian test site. Surface topography in the finite-difference grid was modeled using a vacuum-to-solid density taper. Although the method is simple to apply, it was not thoroughly benchmarked and likely requires a densely sampled wavefield to yield accurate results. Fornberg (1988) presented a pseudospectral scheme in which the interior of the finite-difference grid is deformed to match exactly smooth internal boundaries. Tessmer et al. (1992) and Carcione and Wang (1993) employed an elegant solution to the free-surface problem by isolating the incoming characteristic modes near the surface and calculating the outgoing modes by scaling the incoming modes in accordance with the impedance contrast. By combining this pseudospectral technique with the scheme presented in Fornberg (1988), they accurately modeled wave propagation near a free surface with topography. Hestholm and Ruud (1994) used Fornberg's (1988) technique and a free-surface condition similar to that of Vidale and Clayton (1986) to model wave propagation in the presence of topography on a staggered finite-difference grid. Based on an image method, a fundamentally new approach for modeling irregular free-surfaces is presented in this paper.

Elastic wave propagation is a special case of viscoelastic wave propagation. My discussion of the free-surface condition will, therefore, be concerned with the more general viscoelastic case. I focus on implementations in staggered finite-difference grids (Virieux, 1986; Levander, 1988) and employ an $O(2, 4)$ accurate viscoelastic finite-difference scheme for the simulations (Robertsson et al., 1994). To make the clearest presentation, the 2-D case is illustrated throughout the paper. Generalization

Manuscript received by the Editor August 29, 1995; revised manuscript received March 4, 1996.

*Formerly Institute of Geophysics, Swiss Federal Institute of Technology, ETH-Honggerberg, CH-8093 Zurich, Switzerland; presently Schlumberger Cambridge Research Ltd., High Cross Madingly Rd., Cambridge CB3 0EL, England.

© 1996 Society of Exploration Geophysicists. All rights reserved.

Reprinted from Geophysics, 61, 1921-1934. © 1996 Society of Exploration Geophysicists

to 3-D should be relatively straightforward and obvious from the 2-D description.

I begin by defining the viscoelastic free surface. Several implementations of flat horizontal free-surface approximations are benchmarked against an analytical solution (Sherwood, 1958). A goal of this work is to establish the accuracy of different free-surface implementations and to determine criteria for how finely the wavefield should be sampled. I then present a new algorithm for implementing a free-surface approximation in the presence of topography, which is based on one of the flat free-surface approximations. The algorithm is benchmarked and finally two examples are presented to demonstrate its fidelity.

THE FREE-SURFACE CONDITION

Robertsson et al. (1994) presented a finite-difference scheme to solve the first-order linear partial differential equations describing viscoelastic wave propagation on a staggered grid. For the 2-D case, the following three sets of equations are solved:

Equations governing particle velocity:

$$\begin{cases} \frac{\partial v_x}{\partial t} = \frac{1}{\rho} \left(\frac{\partial \sigma_{xx}}{\partial x} + \frac{\partial \sigma_{xz}}{\partial z} \right) \\ \frac{\partial v_z}{\partial t} = \frac{1}{\rho} \left(\frac{\partial \sigma_{xz}}{\partial x} + \frac{\partial \sigma_{zz}}{\partial z} \right) \end{cases} \quad (1)$$

Equations governing the stress tensor:

$$\begin{cases} \frac{\partial \sigma_{xz}}{\partial t} = \mu \frac{\tau_\epsilon^s}{\tau_\sigma} \left(\frac{\partial v_x}{\partial z} + \frac{\partial v_z}{\partial x} \right) + r_{xz} \\ \frac{\partial \sigma_{xx}}{\partial t} = \pi \frac{\tau_\epsilon^p}{\tau_\sigma} \left(\frac{\partial v_x}{\partial x} + \frac{\partial v_z}{\partial z} \right) - 2\mu \frac{\tau_\epsilon^s}{\tau_\sigma} \frac{\partial v_z}{\partial z} + r_{xx} \\ \frac{\partial \sigma_{zz}}{\partial t} = \pi \frac{\tau_\epsilon^p}{\tau_\sigma} \left(\frac{\partial v_x}{\partial x} + \frac{\partial v_z}{\partial z} \right) - 2\mu \frac{\tau_\epsilon^s}{\tau_\sigma} \frac{\partial v_x}{\partial x} + r_{zz} \end{cases} \quad (2)$$

Equations governing the so-called memory variables, which are introduced to eliminate the numerically inconvenient convolution arising in the viscoelastic constitutive relation:

$$\begin{cases} \frac{\partial r_{xz}}{\partial t} = -\frac{1}{\tau_\sigma} \left(r_{xz} + \mu \left(\frac{\tau_\epsilon^s}{\tau_\sigma} - 1 \right) \left(\frac{\partial v_x}{\partial z} + \frac{\partial v_z}{\partial x} \right) \right) \\ \frac{\partial r_{xx}}{\partial t} = -\frac{1}{\tau_\sigma} \left(r_{xx} + \pi \left(\frac{\tau_\epsilon^p}{\tau_\sigma} - 1 \right) \left(\frac{\partial v_x}{\partial x} + \frac{\partial v_z}{\partial z} \right) - 2\mu \left(\frac{\tau_\epsilon^s}{\tau_\sigma} - 1 \right) \frac{\partial v_z}{\partial z} \right) \\ \frac{\partial r_{zz}}{\partial t} = -\frac{1}{\tau_\sigma} \left(r_{zz} + \pi \left(\frac{\tau_\epsilon^p}{\tau_\sigma} - 1 \right) \left(\frac{\partial v_x}{\partial x} + \frac{\partial v_z}{\partial z} \right) - 2\mu \left(\frac{\tau_\epsilon^s}{\tau_\sigma} - 1 \right) \frac{\partial v_x}{\partial x} \right) \end{cases} \quad (3)$$

In these equations, σ_{ij} denotes the ij th component of the symmetric stress tensor; v_i the i th component of the particle velocity; r_{ij} the memory-variables; τ_ϵ^p and τ_ϵ^s the viscoelastic strain relaxation times for the P - and SV -waves, respectively (Robertsson et al., 1994); τ_σ the viscoelastic stress relaxation

time for both the P - and SV -waves (Robertsson et al., 1994); ρ the density; μ the relaxation modulus corresponding to SV -waves and is the analog of the Lamé constant μ in the elastic case; and π is the relaxation modulus corresponding to P -waves, which is analogous to $\lambda + 2\mu$ in the elastic case, where λ and μ are the Lamé constants.

In 2-D, the viscoelastic free-surface satisfies the following conditions:

$$\begin{cases} \sigma_{iz} = 0 \\ r_{iz} = 0 \end{cases} \quad i = x, z \quad (4)$$

or equivalently from equations (2) and (4):

$$\begin{cases} \frac{\partial v_x}{\partial z} = -\frac{\partial v_z}{\partial x} \\ \frac{\partial v_z}{\partial z} = -\left(1 - 2\frac{\tau_\epsilon^s}{\tau_\epsilon^p} \frac{\mu}{\pi}\right) \frac{\partial v_x}{\partial x} \end{cases} \quad (5)$$

In this paper, the viscoelastic equations described by equations (1), (2), and (3) are constrained along a continuous boundary so that the free-surface conditions described by either equations (4) or (5) are satisfied.

HORIZONTAL FREE-SURFACE APPROXIMATIONS

Suppose that the staggering of the finite-difference grid is implemented such that σ_{xx} , σ_{zz} , r_{xx} , and r_{zz} are located in the upper left corner of the staggered grid cells, v_x immediately to the right, v_z immediately below, and σ_{xz} and r_{xz} are situated in the lower right corner of the grid cells (see for example Figure 3).

Direct method

The most obvious way to implement a free surface condition is to constrain the solution by applying equations (5) directly at the free surface. In this fashion, the free surface can only be implemented to first- or second-order accuracy. In a staggered grid, it can be shown that a stable and explicit free surface may be achieved using equations (5). To my knowledge, it is not possible to implement the constraints so that the free-surface condition is applied only at one level in a staggered grid, i.e., the free surface is applied both at $z = 0$ and $z = \Delta z/2$, where Δz is the grid-size in the depth direction. Hestholm and Ruud (1994) used an eighth-order accurate finite-difference scheme and implemented this type of free-surface condition by successively lowering the accuracy of the scheme toward the surface. I tried several different variations, many of which proved to be unstable or inaccurate. The implementation presented here has the upper part of the free surface through the v_z , σ_{xz} , and r_{xz} components and incorporates appropriate constraints on the particle velocity, stress, and memory variables.

Image methods

A surface of acoustic pressure release is implemented readily through the method of images. Levander (1988) first proposed the use of image techniques to approximate an elastic free surface. The method is based on intuitive arguments and still lacks a rigorous theoretical basis. The idea is as follows: First, choose the geometry so that the free surface is located *exactly* through the upper part of the staggered grid-points at $z = 0$; that is,

σ_{xx} , σ_{zz} , r_{xx} , r_{zz} , and v_x are located on the free surface. To update the wavefield in the proximity of the free surface using a stencil of arbitrary accuracy, both the particle velocity and the stress on several rows of grid-points above the free surface are required. At $z = 0$, σ_{zz} and r_{zz} equal zero. To honor the free-surface condition, σ_{xx} and r_{xx} are updated using only horizontal derivatives of the velocities through equation (5). No vertical derivatives of σ_{xx} occur in the update of the particle velocity. Only the σ_{zz} and σ_{xz} components are needed therefore above the free surface. By imaging both these fields as odd functions around the free surface, we are assured that both fields are zero there.

Three methods of determining particle velocities above the free surface are described here.

Image method 1.—Levander (1988) proposed to update the velocity components above the free-surface using second-order accurate finite-difference approximations of equation (5). Comparison of simulation results with the analytic solution in Sherwood (1958) showed excellent agreement (Levander, 1988).

Image method 2.—Crase (1990) proposed an image technique for updating the particle displacements. He suggested that particle displacement components should be mirrored as even functions. This implies that the particle velocity components should also be even functions with respect to the free surface. From equation (5) it follows that this is not the case. However, both Crase (1990) and Rodrigues and Mora (1993) successfully employed this method.

Image method 3.—The excellent results achieved using the image techniques described previously suggest that free-surface implementations are quite robust, as long as the stress-tensor components are imaged according to the procedure suggested in Levander (1988). I therefore propose a new image method, that is, the particle velocity is set to zero on all rows above the free surface, which is a physically reasonable condition.

Benchmark tests

A semi-infinite elastic medium (Q_P and Q_S of 10 000) with a horizontal free surface was chosen as a test model. The P - and S -velocities are 3000 and 1730 m/s, respectively, and the density 2500 kg/m³ (a Poisson solid). The source is a 15 Hz Ricker wavelet that excites the horizontal component of particle velocity at a point on the free surface. The different free-surface implementations were benchmarked against an analytical solution as given in Sherwood (1958). Time series were recorded at 30 m below the free surface at 1000 and 2000 m source-receiver offset, respectively. The results are presented mainly in terms of the horizontal component of particle velocity, since the direct wave close to the free surface (the same depth as the horizontally acting source) predominantly comprises P -wave motion.

All benchmark tests were performed at a constant maximum (elastic) Courant number of approximately 0.4. The spatial discretization varied from 2 m to 15 m. Results from two free-surface implementations (the direct method and image method 3) are compared to the analytic solution in Figures 1a

and b. The results using image method 3 are closer to the analytical solution than those of the direct method. The latter also models the direct wave inaccurately since the free-surface is implemented at two different levels in a staggered grid-formulation.

The cross-correlation of the simulated time series with the analytical solution may be used as a measure of accuracy. The fit is quantified through: (1) the offset of the main lobe in the cross-correlation from zero lag, and (2) the relative difference in amplitude of the main lobe in the cross-correlation compared to the auto-correlation of the analytical solution. These two measures quantify the numerical dispersion as well as the distortion because of inaccurate modeling of the free

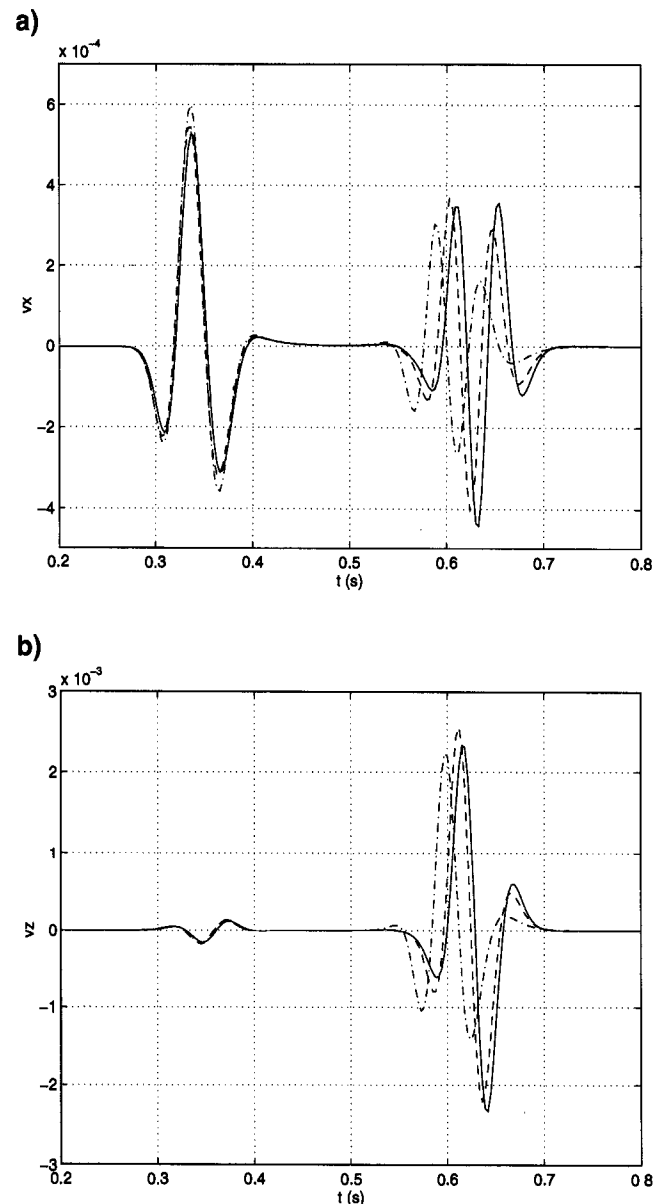


FIG. 1. Time series collected at 30 m depth with a source-receiver offset of 1000 m. (a) Horizontal component of particle velocity. (b) Vertical component of particle velocity. A spatial discretization of 5 m was used in both FD simulations. Source: Ricker wavelet with 15 Hz center-frequency. Solid: analytical solution according to Sherwood (1958). Dash-dotted: FD solution using the direct method. Dashed: FD solution using image method 3.

surface. Parts of the time series corresponding to the arrival of the direct P -wave and the slower waves (predominantly the Rayleigh wave) have been analyzed separately. Overall, the results from all three image techniques display similar accuracies, superior to those of the direct method (Tables 1 to 4).

Assuming that the source has a maximum frequency content of 30 Hz, a 15 m discretization of the finite-difference grid yields a minimum of 6.7 grid-points per wavelength for the P -waves (wavelength of 100 m). This is close to the rule-of-thumb for the minimum number of grid-points per wavelength required for an $O(2, 4)$ accurate finite-difference solution (Levander, 1988). Table 3 shows that for the direct P -wave at 2000 m, a discretization of 15 m yields a maximum two-sample shift (6 ms) of the cross-correlation and a maximum deviation of 7–8% relative to the level of the main lobe in the autocorrelation of the analytical solution.

The inaccuracy of the P -waves at 2000 m source-receiver offset can be used as an estimate of what inaccuracy of the surface waves that can be tolerated at 1000 m (since the velocity of the Rayleigh wave in a Poisson solid is 0.92 times the S -velocity or close to half the P -velocity). Table 2 shows that this level of inaccuracy is reached for the surface waves at a grid-spacing of

Table 1. P -wave. v_x -component at 30 m depth and 1000 m source-receiver offset. Relative difference of cross-correlation between finite-difference (FD) and analytic solution and auto-correlation function of analytic solution. The first value in each field denotes the number of time steps (3 ms/time step) that the main lobe of cross-correlation is shifted relative to zero lag. The second value denotes the percent difference between the amplitude of the main lobe in the cross-correlation compared to the autocorrelation.

Δx (m)	Image 1	Image 2	Image 3	Direct method
15	2/4%	2/5%	2/5%	1/27%
10	1/3%	1/4%	1/4%	0/18%
5	0/1%	0/1%	0/1%	0/11%
2	0/1%	0/1%	0/1%	0/8%

Table 2. Rayleigh wave. v_x -component at 30 m depth and 1000 m source-receiver offset. See caption of Table 1 for details.

Δx (m)	Image 1	Image 2	Image 3	Direct method
15	6/–37%	4/–35%	5/–38%	9/–66%
10	4/–26%	3/–20%	4/–22%	9/–53%
5	2/–9%	1/–7%	1/–8%	6/–35%
2	1/–1%	1/1%	1/1%	3/–14%

Table 3. P -wave. v_x -component at 30 m depth and 2000 m source-receiver offset. See caption of Table 1 for details.

Δx (m)	Image 1	Image 2	Image 3	Direct method
15	2/6%	2/7%	2/8%	1/36%
10	1/3%	1/4%	1/5%	0/23%
5	1/2%	1/2%	1/2%	0/13%

Table 4. Rayleigh wave. v_x -component at 30 m depth and 2000 m source-receiver offset. See caption of Table 1 for details.

Δx (m)	Image 1	Image 2	Image 3	Direct method
15	10/–43%	6/–40%	7/–43%	19/–72%
10	7/–36%	5/–24%	6/–26%	17/–59%
5	3/–12%	3/–10%	3/–10%	12/–47%

5 m. I conclude that a similar rule of thumb applies (possibly somewhat more conservative) for the choice of the number of grid-points per wavelength for the surface waves as for modeling wave propagation in a body with $O(2, 4)$ schemes when using one of the image methods. That is, the image techniques do not appear to introduce inaccuracies larger than those inherent in the $O(2, 4)$ accurate finite-difference scheme. From Tables 2 and 4 it follows that the inaccuracy at 5 m spatial discretization when using the direct method is as severe (or worse) as the inaccuracy at 15 m spatial discretization when using the image methods.

Because of its simplicity and excellent performance, image method 3 was investigated further. It was found to be stable and to produce accurate results for all cases tested with Poisson's ratios from 0 to 0.5. In Figures 2a and 2b, a comparison with the analytical solution for a Poisson's ratio of zero (P -velocity of 3000 m/s, S -velocity of 2121 m/s, and density of 2500 kg/m³) is shown. Since the Poisson's ratio is extreme and the source is located at the free-surface, the Rayleigh wave is strongly excited, representing a thorough test of the free-surface approximation. The excellent performance of this free-surface condition was confirmed in other test cases.

A FREE-SURFACE APPROXIMATION IN THE PRESENCE OF TOPOGRAPHY

An efficient approximation of a free-surface boundary condition along surfaces with topography may be implemented using an image technique. This can be viewed as a generalization of image method 3 for the horizontal free surface. That the velocities may be set to zero above the surface proves to be an important property. Moreover, imaging of the memory variables is not necessary since no spatial derivatives of these occur in equations (1), (2), and (3). The memory variables are treated as the corresponding stress components along the free-surface interface.

The algorithm is presented for irregular free surfaces without over-hanging structures. However, there is nothing that prevents the algorithm from being generalized to also allow for this case.

Descriptions of the staggered grid in the vicinity of the free-surface are shown in Figures 3a and 3b, for a crest and a trough, respectively. The free surface has been discretized such that all grey grid cells belong to it. It is critical where the boundary is located within the staggered grid cells. Numerically, the free surface itself is located along the thick black line. Although numerous alternatives were investigated, only the one presented here leads to stable results that converge to an accurate solution with decreasing spatial step size. The staggering of the grid causes the free surface to have an apparent asymmetric nature. However, when viewed from the perspective of the individual staggered components, the free surface is completely symmetric. The grid-points along the discretized boundary belong to one and only one of the seven following categories: (1) horizontal boundary (H), (2) vertical boundary with air (or rather a vacuum) to the left (VL), (3) inner corner with air above to the left (IL), (4) outer corner with air below to the left (OL), (5) vertical boundary with air to the right (VR), (6) inner corner with air above to the right (IR), and (7) outer corner with air below to the right (OR).

It is worthwhile to recall the physical meaning of the imaging technique. The imaging is performed to ensure that the normal

and shear stresses perpendicular to the boundary under consideration (σ_{zz} and σ_{xz} for the 2-D case of a flat horizontal surface) are zero. Notice that within all seven categories of boundary grid cells, the free surface is always parallel to the grid. Imaging, therefore, only takes place in the directions of the x - and z -coordinate axes. The imaging algorithm is thus reduced to a simple and computationally inexpensive mirroring scheme.

What happens in the vicinity of inner corners, where grid points are subject to imaging from different directions? Briefly, by calculating separately the vertical and horizontal derivatives of the stress components in the update of the particle velocities, such problems are readily avoided (see below).

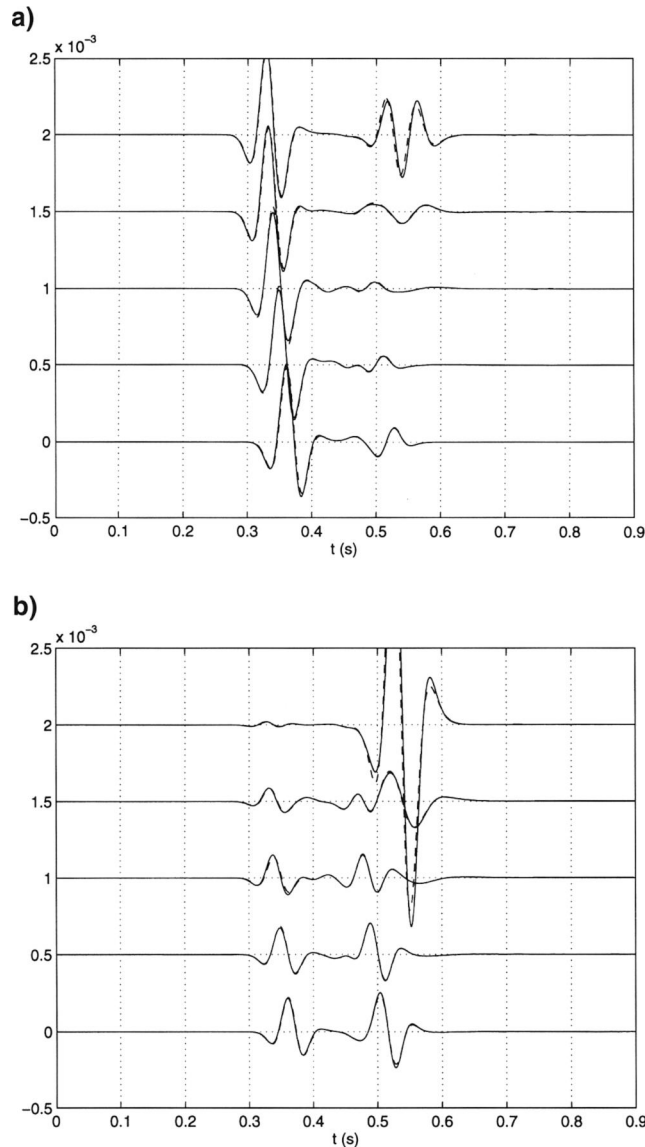


FIG. 2. Time series collected at depths (from above) of 50 m, 150 m, 250 m, 350 m, and 450 m in a medium with Poisson's ratio equal to 0. (a) Horizontal component of particle velocity. Source: Ricker wavelet with 15 Hz center-frequency. Source-receiver offset: 1000 m. A spatial discretization of 5 m was used in the FD simulations. Solid: analytical solution according to Sherwood (1958). Dashed: FD solution using image method 3.

Horizontal boundary grid point (H-point).—An H-point has one neighbor on either horizontal side that is either an H-, OL-, OR-, IL- or IR-point. The H-points are treated identically to image method 3 (the flat free-surface approximation that was described above). Imaging only takes place in the vertical direction. The σ_{xx} and r_{xx} components are thus updated using the fourth-order accurate central finite-difference approximation along the surface.

Vertical boundary grid point with air to the left (VL-point).—A VL-point has one neighbor on either vertical side that is either a VL-, IL- or OL-point. The VL-points are treated similar to the H-points with the exception that here it is the σ_{xx} and r_{xx} components that should be zero at the boundary, and the imaging therefore only takes place in the horizontal direction. The σ_{zz} and r_{zz} components are updated in the same way that the σ_{xx} and r_{xx} components are updated for the H-points.

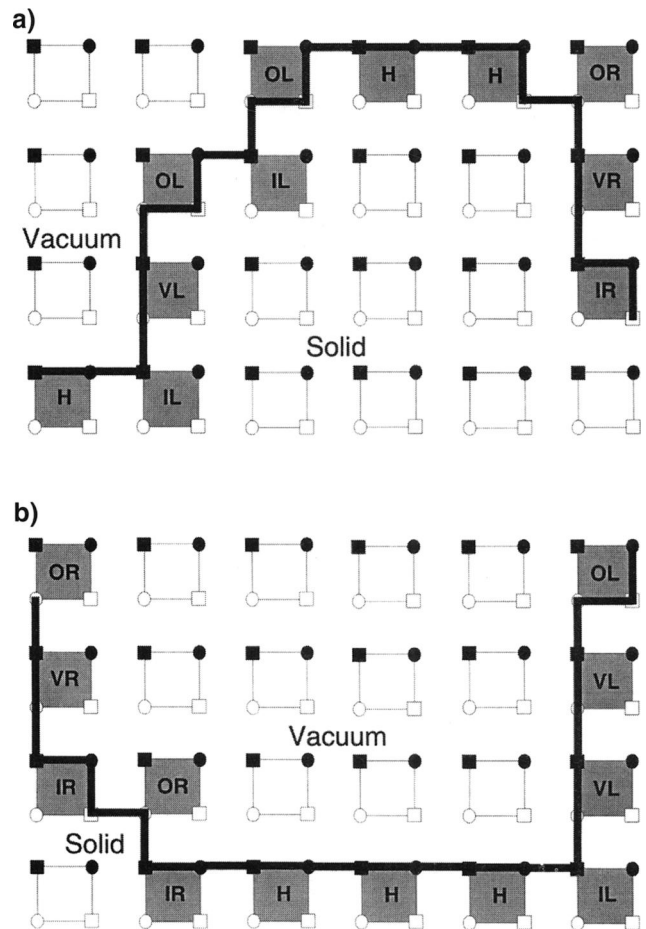


FIG. 3. Staggered finite-difference grid in the vicinity of the free-surface boundary where it either forms (a) a crest or (b) a trough. The light large squares represent the locations of the grid cells. The grid cells colored grey are located along the free-surface boundary, which runs *exactly* along the thick black line. All boundary grid points are classified H-, VL-, IL-, OL-, VR-, IR-, or OR-points as described in the text. Within the grid-cells, the solid squares represent the σ_{xx} , σ_{zz} , r_{xx} , and r_{zz} components, the light squares the σ_{xz} and r_{xz} components, the solid circles the v_x components, and the light circles represent the v_z components.

Inner corner grid point with air above to the left (IL-point).—An IL-point has one neighbor vertically above that is either an OL- or VL-point, and one horizontally to the left that is either an H- or OL-point. No imaging takes place around the IL-points. The σ_{xx} , σ_{zz} , r_{xx} , and r_{zz} components are located along the boundary, perpendicular to parts of it, and are therefore set to zero.

Outer corner grid point with air to the left (OL-point).—An OL-point has either an IL- or H-point immediately to the right and an IL- or VL-point immediately below. The free surface is located through the v_x , v_z , σ_{xz} and r_{xz} components, while the normal stresses and the corresponding memory variables are located in the air above the free-surface (Figure 3). The σ_{xz} and r_{xz} components are therefore set to zero. The σ_{xx} and σ_{zz} components are imaged horizontally with respect to the far right vertical part of the free surface, and the σ_{zz} and again the σ_{xz} components are imaged vertically with respect to the lowermost horizontal part of the free surface (Figure 3). If the OL-point is adjacent to an IL-point, the particle velocity component in between must be set to zero to obtain a stable and accurate solution.

Vertical boundary grid point with air to the right (VR-point).—A VR-point has one neighbor on either vertical side that is either a VR-, IR- or OR-point. The VR-points are treated analogously to the VL-points, with the exception that the imaging takes place in the opposite horizontal direction.

Inner corner grid point with air above to the right (IR-point).—An IR-point has one neighbor vertically above that is either an OR- or VR-point, and one horizontally to the right that is either an H- or OR-point. Only vertical imaging of the σ_{xz} component takes place for the IR-points. The σ_{xx} , σ_{zz} , r_{xx} , and r_{zz} components are located along the boundary, perpendicular to parts of it, and are therefore set to zero.

Outer corner grid point with air to the right (OR-point).—An OR-point has either an IR- or H-point immediately to the left and an IR- or VR-point immediately below. The free-surface makes a step immediately to the left of the OR-point and only intersects with its v_z component, whereas the other velocity- and stress fields are located in the air above the free surface (Figure 3). The σ_{xz} and r_{xz} components immediately to the left of the boundary point are set to zero. The σ_{xx} and σ_{zz} components are imaged horizontally with respect to the vertical segment of the free-surface boundary to the left of the grid point (Figure 3). The σ_{zz} component is imaged vertically with respect to the step at the v_z component in the OR-point. If the OR-point is adjacent to an IR-point, the particle velocity component in between must be set to zero to obtain a stable and accurate solution.

Implementation

Classification of the free-surface boundary points takes place before the finite-difference calculation begins. Maximum computational efficiency is obtained by setting the reciprocal values of the densities to zero everywhere in the finite-difference grid above the free surface. The particle velocities will then automatically be zero above the free surface after every update [equations (1)].

The staggered stress, memory variable, and particle velocity fields are not only shifted spatially relative to each other but also temporally (Virieux, 1986). The stress components [equations (2)] and memory variables [equations (3)] are updated half a time step after the particle velocity components [equations (1)]. Thus, the particle velocity is updated separately from the other variable fields. In equations (1), each consist of two derivatives (one vertical and one horizontal) of stress tensor components. By first performing all vertical imaging of the stress components (H-, OR-, OL-, and IR-points) and then calculating and adding only the vertical derivatives in equations (1), the free-surface condition is satisfied completely in all grid-cells along the boundary. Next, the horizontal imaging of the stress components (VL-, VR-, OR-, and OL-points) is performed followed by an update with the remaining horizontal derivatives in equations (1), again satisfying the free-surface boundary condition. Following the updates of equations (1), it is necessary to set the v_x components to zero in the VR- and OR-points, since the reciprocal velocity is not zero in these points.

Subsequently, the stress-fields [equations (2)] and memory variables [equations (3)] are updated. This action does not involve any imaging of the variable fields. Following the update, the correction of the normal stress and memory variable parallel to the surface must be made at the H- (σ_{xx} and r_{xx}), VL- and VR-points (σ_{zz} and r_{zz}), as described above for the horizontal free-surface.

The imaging algorithm thus does not add a substantial amount of computational cost to the finite-difference calculations. Moreover, the algorithm does not reduce significantly the degree of vectorization or parallelization of the finite-difference code. However, computations are wasted in the region occupied by air above the topography in the finite-difference grid.

There is a modeling limit as to how narrow the “troughs” or “crests” in the topography can be. A crest cannot be narrower than the number of grid points imaged around its horizontal sides. Figure 3a shows the narrowest crest that is allowed when using fourth-order accurate spatial central-difference approximations. Such a crest must have a top consisting of at least one OL-, two H-, and one OR-point. Within a trough on the other hand, there must be sufficient space to allow for horizontal imaging with respect to its walls. Figure 3b shows the narrowest trough that is allowed for the same scheme. Here, the bottom must consist of at least one IR-, three H-, and one IL-point.

Benchmark tests

A flat semi-infinite elastic medium (Q_P and Q_S of 10 000) was chosen to benchmark the free surface with topography. As before, the test model is a Poisson solid with P - and S -velocities of 3000 and 1730 m/s, respectively, and a density of 2500 kg/m³. For this phase of testing the slope of the surface within the grid was varied. If wave propagation is successfully modeled independent of the slope of the surface, then the algorithm should also allow for accurate modeling of free surfaces with more general shapes.

To avoid problems arising from the uncertainty of where the exact location of the source close to the surface is, an isotropic P -wave source (15 Hz Ricker wavelet) located 30 m below the surface was employed. In the following tests the slopes of the free surface were set to -60° , -45° , -30° , -15° , 0° , 15° ,

30°, 45° and 60°, and the time series were collected at 1000 m source-receiver offset in a direction parallel to the surface. The recorded particle velocities were rotated to the coordinate system of the 0° case, so that all time series may be compared to each other directly. The solution for the 0° slope may be regarded as an approximation to the exact solution, since this has already been benchmarked against the analytical solution of Sherwood (1958) and shown to yield accurate results for the spatial discretizations employed here. The benchmark tests were performed at a maximum (elastic) Courant number of 0.45.

In Figures 4a and 4b, particle velocities from the simulations with the various free-surface slopes are plotted. The time series were collected 50 m below the surface, and a spatial

discretization of 2 m was used. Because of the varying amplitude levels of the recorded time series for different particle velocity components or receiver locations, a different linear scaling factor have been used in the figures. This is indicated in the lower right corner in each figure. The time series are satisfactorily uniform from trace to trace. Figures 4c and 4d show time series from analogous simulations with a spatial discretization of 4 m. Present in these figures are characteristic tails of the Rayleigh waves caused by numerical dispersion. Some components of the tails in Figures 4c and 4d could be caused by “errors” in the rotation of the velocity vector field, since the v_x and v_z components are located 2.8 m from each other within the staggered grid cells. This effect could be substantial, because the strength of the two components

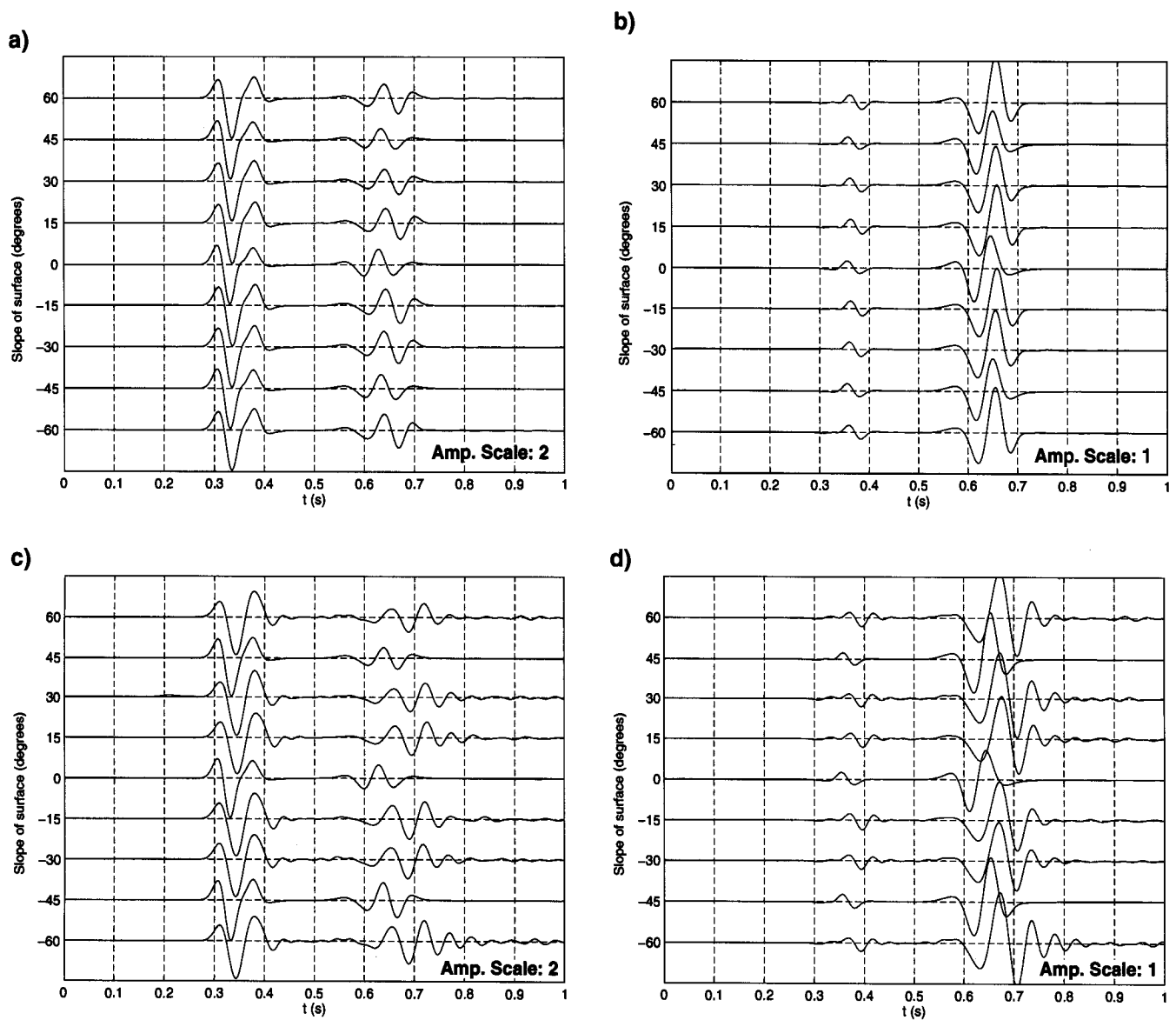


FIG. 4. Time series collected at 50 m below the free surface and 1000 m source-receiver offset. (a) Particle velocity parallel to the free surface. Grid-spacing: 2 m. (b) Particle velocity perpendicular to the free surface. Grid spacing: 2 m. (c) Particle velocity parallel to the free surface. Grid spacing: 4 m. (d) Particle velocity perpendicular to the free surface. Grid spacing: 4 m. The flat free surface intersected the finite-difference grid with angles of 60°, 45°, 30°, 15°, 0°, -15°, -30°, -45° and -60°. The results are better the more alike the traces are to each other within each figure. The scaling factors are shown in the figures. Source: 15 Hz Ricker wavelet at 30 m depth.

differs significantly (taking the scales in Figures 4c and 4d into account). Besides the surface with 0° slope, the $\pm 45^\circ$ slope examples yield the most accurate results.

In Figures 5a to 5d, time series collected at 350 m depth using spatial discretizations of 2 and 4 m are shown. Again, the complex wavetrains are uniform from trace to trace in each figure. No evidence of scattering from the discrete steps along the free surface are observed.

In the presence of topography, approximately at least 15 grid-points per minimum wavelength are required to model the complete wavetrain with sufficient accuracy. This estimate is based on the observation that the modeling of Rayleigh waves with sufficient accuracy breaks down when increasing the spatial sampling from 2 to 4 m in Figures 4a to 4d. Energy

propagating at an angle relative to the grid is actually sampled more sparsely. A Rayleigh wave propagating along a 45° slope in a grid with 4 m discretization experiences a 5.7 m discretization, of course, a similar effect is seen for body waves traveling oblique to the finite-difference grid. The reduced accuracy near the surface topography appears to be caused by the fact that a smooth boundary is represented by finite steps causing scattering (Fuyuki, M., and Matsumoto, Y., 1980). However, attenuation and dispersion may be particularly severe close to the earth's surface. Since the higher frequency components propagate closer to the surface where attenuation is stronger, and since these components also have the shortest wavelengths, less strict criteria may be used for choosing the number of grid points per wavelength for the surface waves.

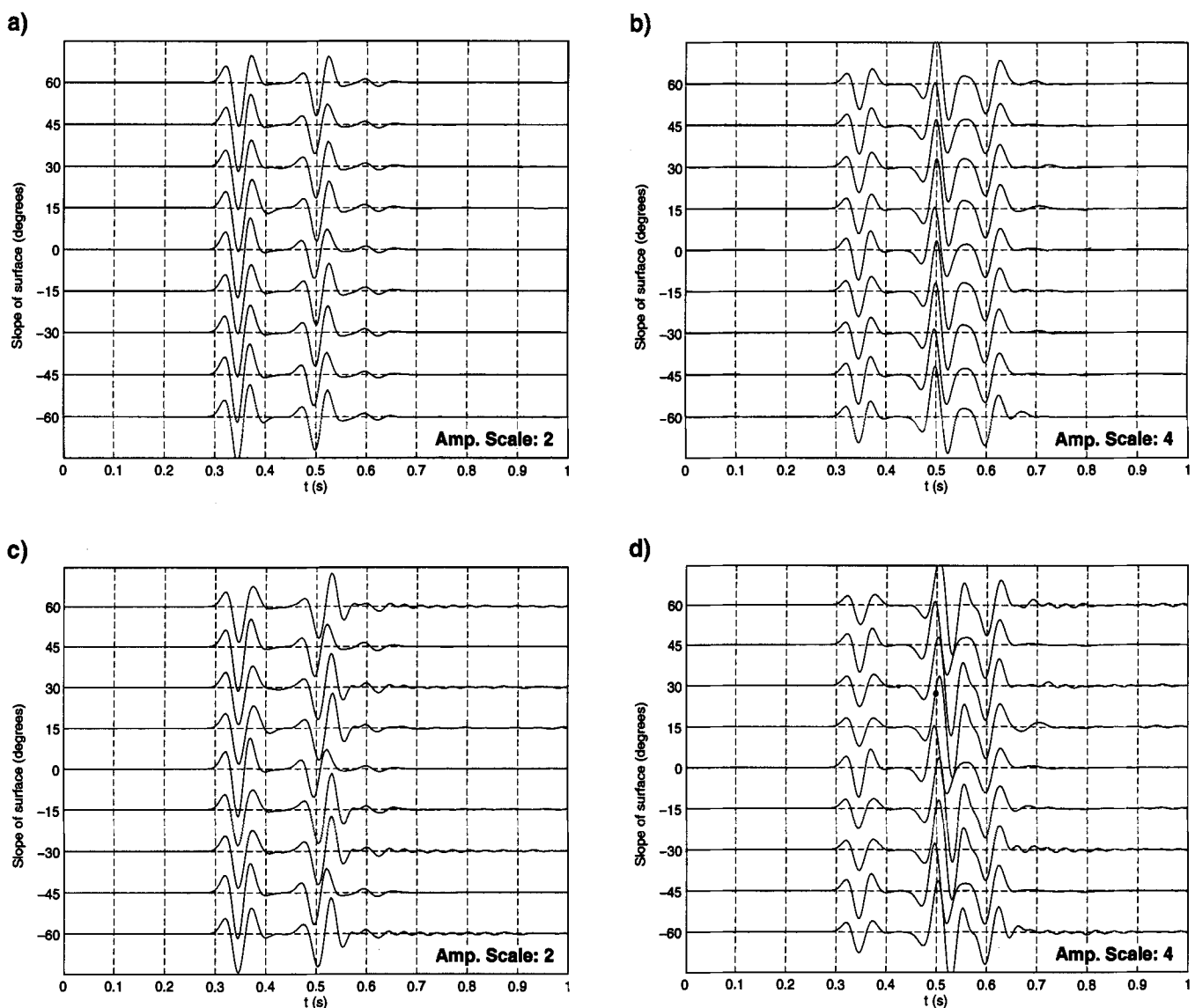


FIG. 5. Time series collected at 350 m below the free-surface and 1000 m source-receiver offset. (a) Particle velocity parallel to the free-surface. Grid spacing: 2 m. (b) Particle velocity perpendicular to the free surface. Grid spacing: 2 m. (c) Particle velocity parallel to the free surface. Grid spacing: 4 m. (d) Particle velocity perpendicular to the free surface. Grid spacing: 4 m. The flat free surface intersected the finite-difference grid with angles of 60° , 45° , 30° , 15° , 0° , -15° , -30° , -45° and -60° . The results are better the more alike the traces are to each other within each figure. The scaling factors are shown in the figures. Source: 15 Hz Ricker wavelet at 30 m depth.

Numerous tests using topography functions of various roughness overlaying media with widely varying Q , and Poisson's ratios from 0 to 0.5 were performed. No instabilities or unreasonably inaccurate results were observed.

EXAMPLES

Two sets of 2-D simulations in which the presence of topography has a significant impact on the seismic response are presented here. In the simulations, absorbing boundaries along the sides and at the bottom of the grid are employed; a low Q frame (i.e., a Q of 2 for both P - and S -waves) that attenuates incoming energy is located around the grid (Robertsson et al., 1994; Blanch et al., 1995). To further reduce the effects of the boundaries, first-order outward radiating absorbing boundary conditions (Higdon, 1991) were applied outside this frame. This combination of absorbing boundary techniques attenuates efficiently the high amplitude direct P -waves, S -waves, Rayleigh waves, etc., which are incident over a wide range of angles. In all snapshots, the absorbing frame, which was chosen typically to be 1–2 times the maximum dominant wavelength, has been omitted.

In the snapshots, energy appears to be concentrated along the topographic surface. This is an artifact of the plotting routine. For the P snapshots, the divergence of the particle velocity field is calculated and for the S snapshots the curl. Since the velocity is zero above the surface, large values appear in the snapshots along the topography.

In the following examples, the results of effective elastic simulations are shown, and quality factors of 10 000 were used. The reason for employing pseudoelastic models is to make the analyses of the simulations easier by not having to account for the effects of attenuation and dispersion.

Example 1: Effects of a smooth topography on seismic data

Two simulations were performed using the model described in Figure 6 and Table 5. A Ricker wavelet with a center-frequency of 30 Hz was used as a pure P -wave source (denoted by a star in Figure 6). Although the model displays dramatic variations in the topography it is referred to as being smooth since the scale of the roughness is large compared to the wavelengths of interest. In the first simulation, the second interface in the model was ignored, so that the entire model below the varying topography is homogeneous with the material properties of medium 2. This model will be referred to as the

“one-layer” model. For the second simulation, the model as described by Figure 6 and Table 5 was used. In this “two-layer” model, the second interface is located approximately 40 m below the free surface. This is a more realistic model, since the near surface in many regions of the earth is characterized by relatively thin layers with large velocity contrasts and gradients.

In Figures 7a and 7b, snapshots 0.36 and 0.72 s after the initiation of the source using the one-layer model are shown. The topography causes multiple P - and S -wavefronts as the direct P -wave reflects off the free surface. Notice how several Rayleigh wave packages propagate along the free surface (easiest to identify in the S snapshots because of the scaling; e.g., at $x = 500$ m in Figure 7a, and $x = 500$ and 800 m in Figure 7b).

In Figures 8a and 8b, analogous snapshots for the two-layer model are shown. The wavefield is considerably more complicated because of the multiple reflections and channeling of waves in the upper layer. Even though the snapshots have the same major characteristics, the two-layer model produces a much more complex pattern. Notice how almost all of the P -energy has dissipated out of the one-layer model at 0.72 s (Figure 7b), whereas significant energy remains in the two-layer model (Figure 8b). I conclude that a model with relatively smooth topography, a thin near-surface layer, and moderate contrasts in material properties can complicate the wave pattern significantly because of multiple reflections and channeling of the wavefield.

Example 2: Resonances in irregular low-velocity surface layers

In two classic papers, Hill and Levander (1984) and Levander and Hill (1985) investigated the effects that low velocity layers with irregular interfaces have on seismic responses. In particular, Levander and Hill (1985) found that a low-velocity layer with an irregular lower interface could be responsible for the

Table 5. Material properties used in Example 1 with the model in Figure 6.

	Medium 1	Medium 2
P -velocity (m/s)	1700	2200
S -velocity (m/s)	775	1000
Density (kg/m ³)	2000	2300
Q_P	10000	10000
Q_S	10000	10000

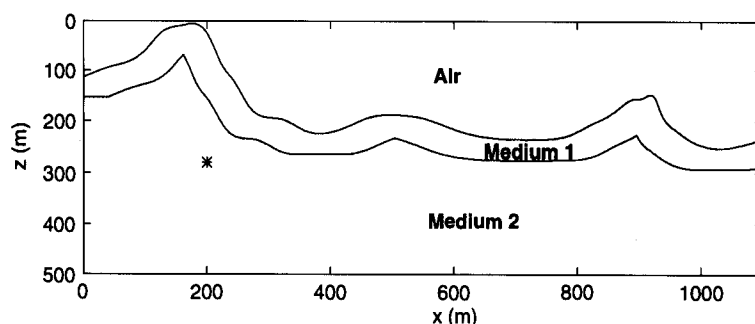


FIG. 6. Example 1: The “two-layer” model. The material properties are listed in Table 5. The interface between medium 1 and medium 2 is always 40 m below the closest point on the surface. The star denotes the location of the 30 Hz Ricker wavelet source. The “one-layer” model is identical to the “two-layer” model, except that the material properties of medium 1 are set equal to those of medium 2.

long complex coda often observed in teleseismic data. Seismic energy propagating vertically from below was shown to scatter into Rayleigh modes of the near-surface waveguide. The trapped energy could then propagate over long distances, while scattering from the irregular lower boundary.

In the top of Figure 9, a model of the type that was used by Levander and Hill (1985) is shown. In this model, which will

be referred to as model A, a horizontal free surface overlays a two-layered model. The upper layer has considerably lower velocities than the lower layer, and the interface between the two layers is rough. This was generated by varying the interface position according to

$$\xi(x) = z_1 + \epsilon(x, n),$$

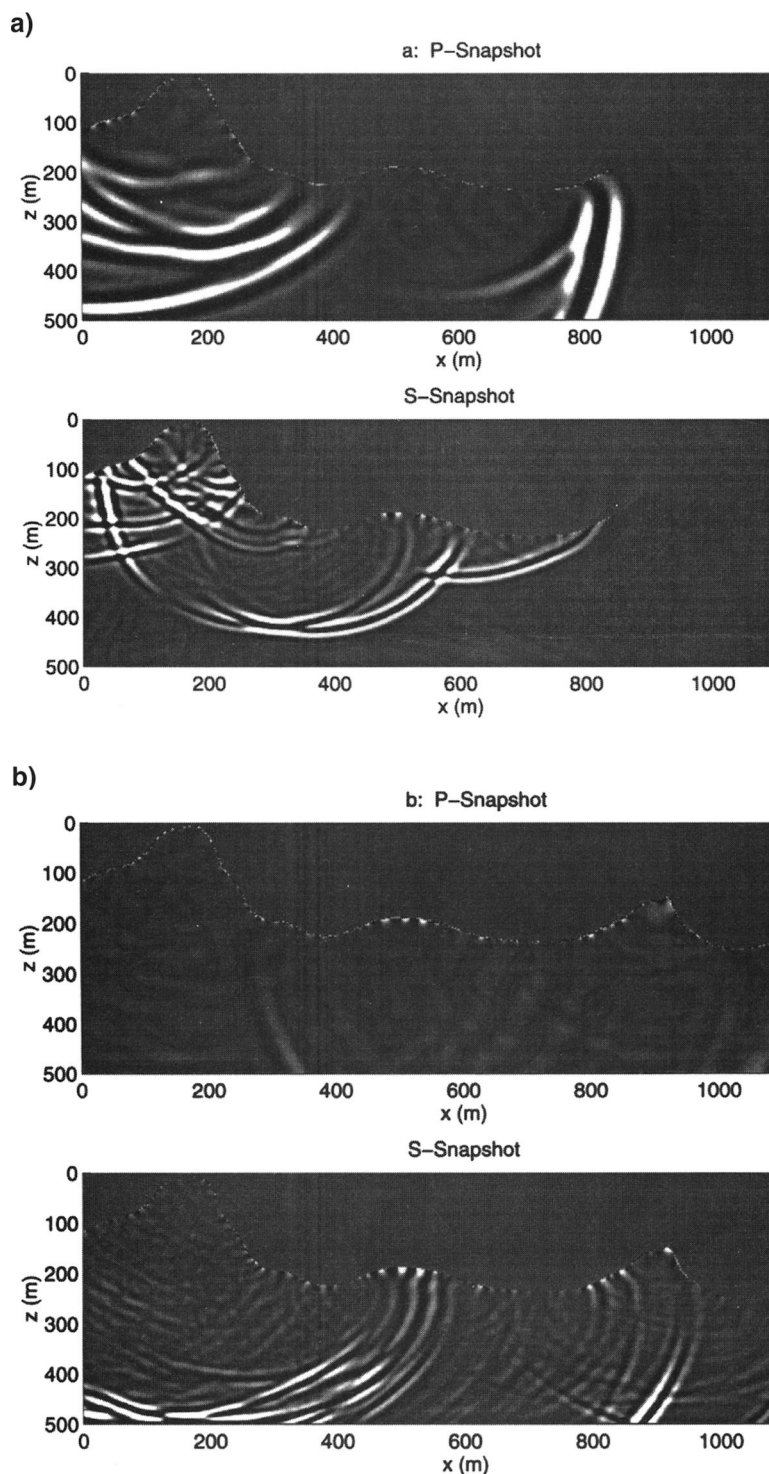


FIG. 7. Example 1: *P*- (above) and *S*-energy (below) snapshots from the simulation using the one-layer model (see Figure 6 and Table 5) at (a) 0.36 s using scaling factors of 1 both for the *P*- and *S*-snapshots. (b) 0.72 s using scaling factors of 8 and 2 for the *P*- and *S*-snapshots, respectively.

where z_1 is the average depth of the rough interface (chosen so that it is located 50 m from the smooth interface), $\epsilon(x, n) = Ar(x/n\Delta x)$, $A = 20$ m is the amplitude, $\Delta x = 2.5$ m is the spatial grid sample, and r is a uniformly distributed random number so that $-1 \leq r \leq 1$. A new random number r is generated whenever the argument $x/n\Delta x$ takes on integral values (Levander and Hill, 1985). To obtain similar models to Levander and Hill (1985) n is chosen to equal 10.

In contrast to model A, the model at the bottom of Figure 9, referred to as model B, has a smooth lower interface whereas the free surface is rough.

In all simulations, the source used was a 10 Hz Ricker plane-wave incident on the low-velocity layer vertically from below. For both models, the wavefield was recorded along a horizontal array located entirely within the low-velocity layer (25 m from the smooth interface).

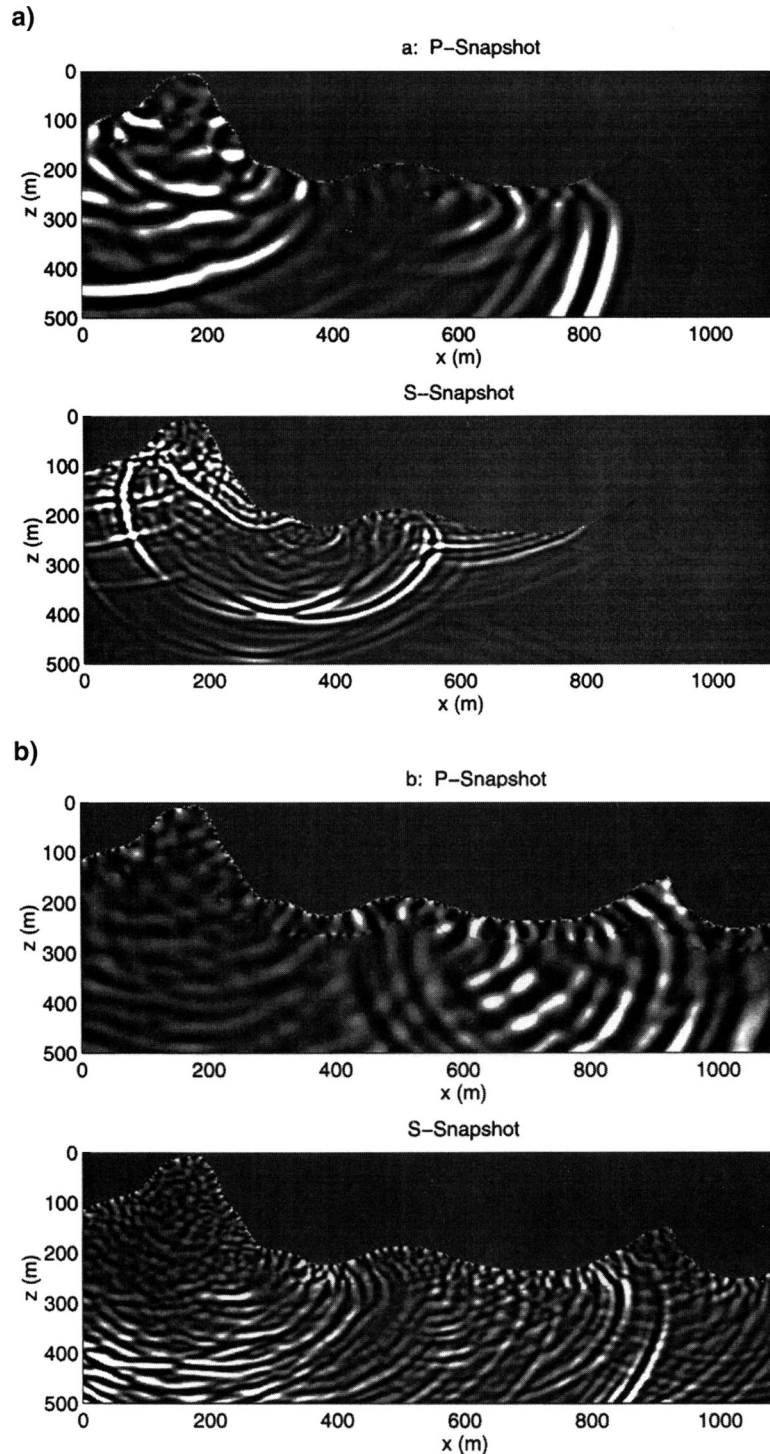


FIG. 8. Example 1: P - (above) and S -energy (below) snapshots from the simulation using the two-layer model (see Figure 6 and Table 5) at (a) 0.36 s using scaling factors of 1 both for the P - and S -snapshots. (b) 0.72 s using scaling factors of 8 and 2 for the P - and S -snapshots, respectively.

In Figure 10, the recorded horizontal particle velocity from the simulation using model A is shown. As shown by Levander and Hill (1985), the strong lineations of the scattered field correspond to the phase-velocity of Rayleigh dispersion. Since the incident wavefield has only vertical motion, these modes can only be excited after scattering from the irregular lower interface of the low-velocity layer.

In Figure 11, the recorded wavefield using model B is shown. Lineations in the scattered field are still present, but overall the wavefield appears slightly more chaotic. The rough topography now scatters energy into the waveguide. Rayleigh waves continue to scatter from the rough free surface.

From 0.4 s to 1.0 s there is 50% more energy in the recorded wavefield from model B compared to model A. This ratio stays constant for later sections of the recorded wavefield. I conclude that rough topography may lead to efficient channeling of the incident plane wave into the low-velocity layer, which then may be observed as "incoherent coda" in recorded data.

DISCUSSION AND CONCLUSIONS

Various finite-difference approximations of flat free surfaces have been tested and benchmarked against an analytical solution (Sherwood, 1958). In addition to the tests described here, several free-surface implementations involving the direct application of equation (5) were attempted. Many of these implementations proved to be unstable or produced inaccurate

results. Conversely, implementations based on image techniques (Levander, 1988) generally proved to be accurate and stable. As long as the stress components are imaged correctly, the choice of particle velocity above the free surface does not seem to be critical. Because of its simplicity, I favor the implementation in which particle velocities are set to zero above the free surface (image method 3).

A new method for modeling wave propagation in the presence of topography has been presented. The technique is an extension of image method 3 to allow for irregular free surfaces. In contrast to methods based on deformations of grids (Fornberg, 1988; Tessmer et al., 1992; Carcione and Wang, 1993; Hestholm and Ruud, 1994), the stability criterion for this new approach is not affected by the presence of topography. Moreover, it is possible to model arbitrarily steep structures using the new technique. A limitation of the method is that very narrow structures cannot be modeled. A minimum of three grid-points are required for troughs and four grid-points for crests. These are not serious limitations, since modeling of such small-scale structures in finite-difference grids, is in itself, questionable.

This new method may be implemented easily in conventional staggered finite-difference schemes. Since updating the particle velocities can be separated into operations involving only vertical or only horizontal derivatives of the stress components, the imaging may be performed without affecting significantly the computational efficiency of the finite-difference scheme.

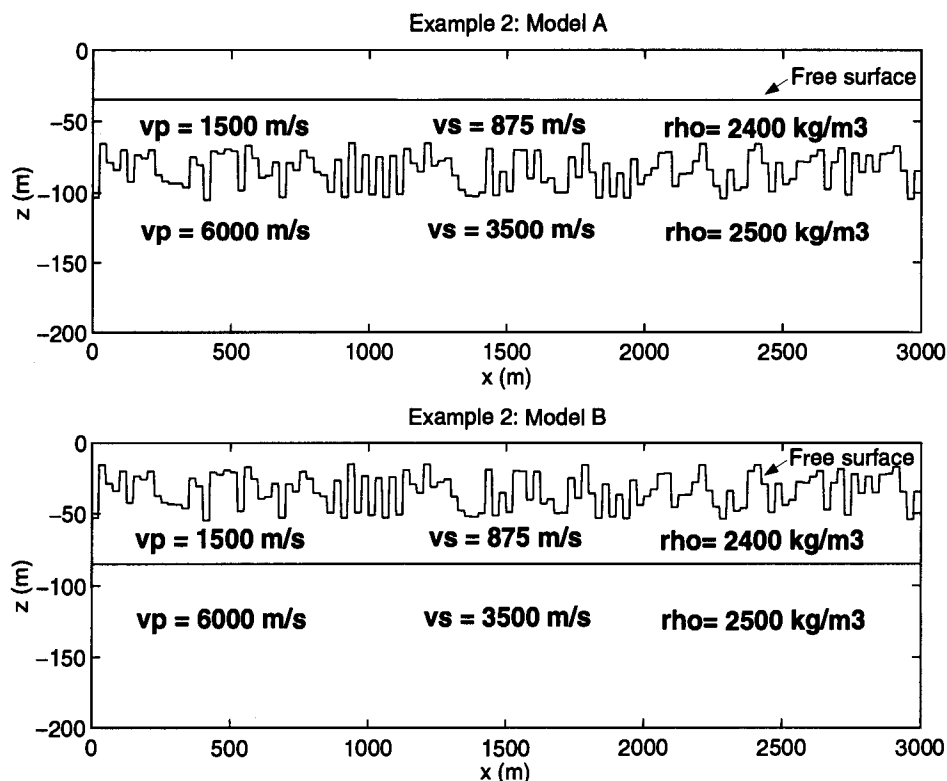


FIG. 9. Example 2: Models A and B used in the simulations. The interface above the medium with a P -velocity of 1500 m/s is the free surface (irregular in Model B). The irregular interfaces are described in the text. Notice that the vertical exaggeration is 5:1.

Updates in the domain above the free surface are wasted computational effort, but enable efficient vectorization and parallelization.

The new method was successfully benchmarked using flat surfaces with varying slopes. Instead of a minimum number of five grid-points per shortest wavelength in the interior of the $O(2, 4)$ accurate finite-difference grid (Robertsson et al., 1994), I found that approximately at least 15 grid-points are required. This reduced accuracy appears to be caused by the fact that the imaging method yields a good representation of a "staircase-shaped" function, whereas a smooth boundary must be discretized in terms of such steps. Fuyuki and Matsumoto (1980) found that scattering of Rayleigh waves can be substantial also from relatively small steps compared to the wavelength. The fact that the $\pm 45^\circ$ cases in the benchmark tests are more accurately modeled than the other cases also points in this direction. Here the steps are finer since the boundary goes through individual grid cells.

Modeling wave propagation along discretized boundaries through finite-difference grids always produces results that are less accurate than simulating wave propagation in homogeneous media. This problem is not unique to the free surface, but occurs at any interface with a discontinuity in material properties. One way of avoiding this problem is to deform the grid (Fornberg, 1988). Muir et al. (1992) describe an alternative technique in which the material properties are averaged in the

vicinity of the irregular boundary, but this approach seems to require finite material properties on both sides of the interface; a vacuum above the free surface would prohibit the use of any interpolation scheme of this category.

Finally, two sets of models in which the topography has a significant impact on the seismic responses were presented. In the first example, it was shown that a near-surface layer under relatively smoothly varying topography may cause a very complex wavefield, largely due to multiple reflections and channeling of waves in the layer. In the second example, I presented simulations similar to those performed by Levander and Hill (1988), in which the effects of a highly irregular near-surface layer were studied. In addition, I investigated the case of very rugged topography overlaying a near-surface low-velocity layer and found that this configuration leads to even more efficient channeling of teleseismic waves into the layer. Scattering from a complex free surface might thus be one of the causes why earthquake coda can generally not be explained by volume scattering only.

ACKNOWLEDGMENTS

I wish to thank Alan Levander, William W. Symes, Klaus Holliger, Joakim O. Blanch, José Carcione, and Stig Hestholm for many discussions and helpful suggestions. Thanks to associate editor Mathew J. Yedlin, John T. Etgen and one anonymous referee for valuable comments and for reviewing the

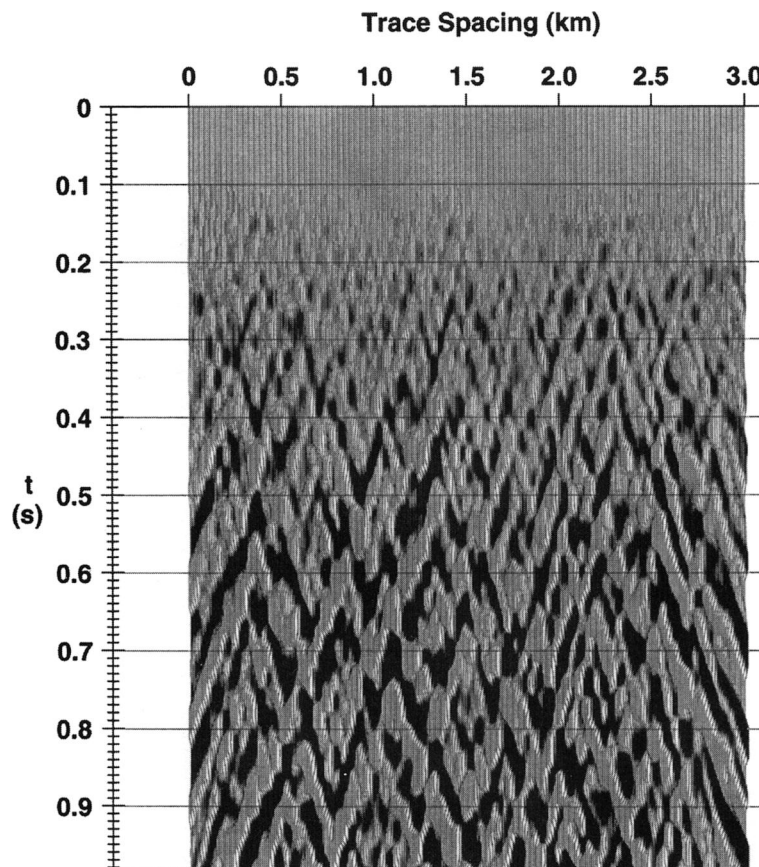


FIG. 10. Example 2: Seismogram (horizontal component of particle velocity) recorded in the simulation using model A (Figure 9).

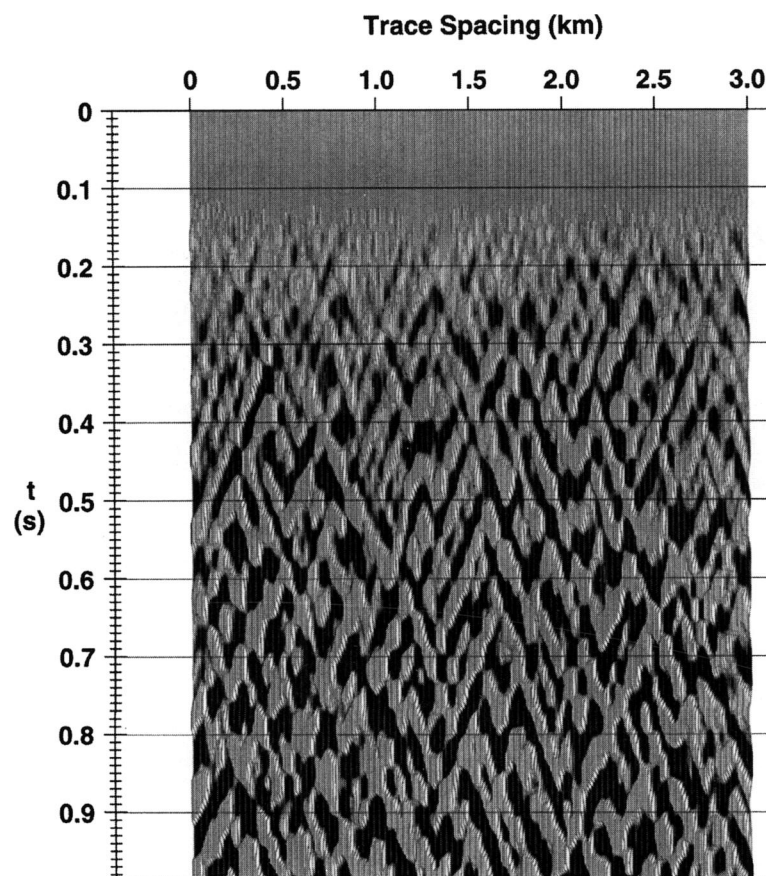


FIG. 11. Example 2: Seismogram (horizontal component of particle velocity) recorded in the simulation using model B (Figure 9).

paper. I thank Alan Green and Anne L. Blume-Robertsson for reading, commenting on, and helping to edit the manuscript. The simulations were performed partly on the Cray YMP at ETH. ETH-Geophysics contr. no. 871.

REFERENCES

- Blanch, J. O., Robertsson, J. O. A., and Symes, W. W., 1995, Modeling of a constant Q : Methodology and algorithm for an efficient and optimally inexpensive viscoelastic technique: *Geophysics*, **60**, 176–184.
- Carcione, J. M., and Wang, J. P., 1993, A Chebyshev collocation method for the elastodynamic equation in generalized coordinates: *Comput. Fluid Dynamics J.*, **2**, 269–290.
- Cohen, G., Joly, P., and Tordjman, N., 1993, Construction and analysis of higher order finite elements with mass lumping for the wave equation: Construction and analysis of higher order finite elements with mass lumping for the wave equation: *Proc. Second Internat. Conf. on Mathematical and Numerical Aspects of Wave Propagation: Soc. for Ind. and Appl. Math.*, 152–160.
- Cruse, E., 1990, High-order (space and time) finite-difference modeling of the elastic wave equation: High-order (space and time) finite-difference modeling of the elastic wave equation: 60th Ann. Internat. Mtg., Soc. Expl. Geophys., Expanded Abstracts, 987–991.
- Fornberg, B., 1988, The pseudospectral method: Accurate representation of interfaces in elastic wave calculations: *Geophysics*, **53**, 625–637.
- Frankel, A., and Leith, W., 1992, Evaluation of topographic effects on P - and S -waves of explosions at the northern Novaya Zemlya test site using 3-D numerical simulations: *Geophys. Res. Lett.*, **19**, 1887–1890.
- Fuyuki, M., and Matsumoto, Y., 1980, Finite-difference analysis of Rayleigh wave scattering at a trench: *Bull. Seis. Soc. Am.*, **70**, 2051–2069.
- Hestholm, S. O., and Ruud, B. O., 1994, 2-D finite-difference elastic wave modeling including surface topography: *Geophys. Prosp.*, **42**, 371–390.
- Higdon, R. L., 1991, Absorbing boundary conditions for elastic waves: *Geophysics*, **56**, 231–241.
- Hill, N. R., and Levander, A. R., 1984, Resonances of low-velocity layers with lateral variations: *Bull. Seis. Soc. Am.*, **74**, 521–537.
- Jih, R. S., McLaughlin, K. L., and Der, Z. A., 1988, Free-boundary conditions of arbitrary polygonal topography in a two-dimensional explicit elastic finite-difference scheme: *Geophysics*, **53**, 1045–1055.
- Levander, A. R., 1988, Fourth-order finite-difference P - SV seismograms: *Geophysics*, **53**, 1425–1436.
- Levander, A. R., and Hill, N. R., 1985, P - SV resonances in irregular low-velocity surface layers: *Bull. Seis. Soc. Am.*, **75**, 847–864.
- Muir, F., Dellinger, J., Etgen, J., and Nichols, D., 1992, Modeling elastic fields across irregular boundaries: *Geophysics*, **57**, 1189–1193.
- Robertsson, J. O. A., Blanch, J. O., and Symes, W. W., 1994, Viscoelastic finite-difference modeling: *Geophysics*, **59**, 1444–1456.
- Rodrigues, D., and Mora, P., 1993, An efficient implementation of the free-surface boundary condition in 2-D and 3-D elastic cases: An efficient implementation of the free surface boundary condition in 2-D and 3-D elastic cases: 63rd Ann. Internat. Mtg., Soc. Expl. Geophys., Expanded Abstracts, 215–217.
- Sherwood, J. W. C., 1958, Elastic wave propagation in a semi-infinite solid medium: *Proc. of the Physical Soc.*, **71**, 207–219.
- Strang, G., and Fix, G. J., 1973, An analysis of the finite element method: Prentice-Hall.
- Tessmer, E., Kosloff, D., and Behle, A., 1992, Elastic wave propagation simulation in the presence of surface topography: *Geophys. J. Int.*, **108**, 621–632.
- Vidale, J. E., and Clayton, R. W., 1986, A stable free-surface boundary condition for two-dimensional elastic finite-difference simulation: *Geophysics*, **51**, 2247–2249.
- Virieux, J., 1986, P - SV wave propagation in heterogeneous media: Velocity-stress finite-difference method: *Geophysics*, **51**, 889–901.